ACS APPLIED MATERIALS & INTERFACES

Research Article

Cite This: ACS Appl. Mater. Interfaces 2018, 10, 34744−34750

www.acsami.org

Investigation of Interface Effect on the Performance of $CH_3NH_3PbCl_3$/ZnO UV Photodetectors

Jialin Yang,[†,‡] Kewei Liu,[*,†] Zhen Cheng,[†,‡] Pengtao Jing,[†] Qiu Ai,[†,‡] Xing Chen,[†] Binghui Li,[†] Zhenzhong Zhang,[†] Ligong Zhang,[†] Haifeng Zhao,[†] and Dezhen Shen[*,†]

[†]State Key Laboratory of Luminescence and Applications, Changchun Institute of Optics, Fine Mechanics and Physics, Chinese Academy of Sciences, Changchun 130033, People's Republic of China

[‡]University of Chinese Academy of Sciences, Beijing 100049, People's Republic of China

Supporting Information

ABSTRACT: Recent investigations indicate that the performance of organic−inorganic perovskite optoelectronic devices can be improved by combining the perovskites and the inorganic materials. However, very few studies have focused on the investigation of perovskites/inorganic semiconductor hybrid UV photodetectors and their detailed performance-enhancement mechanism is still not very clear. In this work, a $CH_3NH_3PbCl_3$/ZnO UV photodetector has been first demonstrated and investigated. Both the photoresponsivity and response speed of the hybrid device are higher than those of pure $CH_3NH_3PbCl_3$ and ZnO devices. The photoluminescence and transient absorption spectra indicate that the photoinduced electron transfer between $CH_3NH_3PbCl_3$ and ZnO should be responsible for the performance enhancement of the hybrid device. In addition, the high crystal quality of $CH_3NH_3PbCl_3$ on ZnO film is another important reason for the excellent UV detection performance. Our findings in this work provide new insights into the intrinsic photophysics essential for perovskite optoelectronic devices.

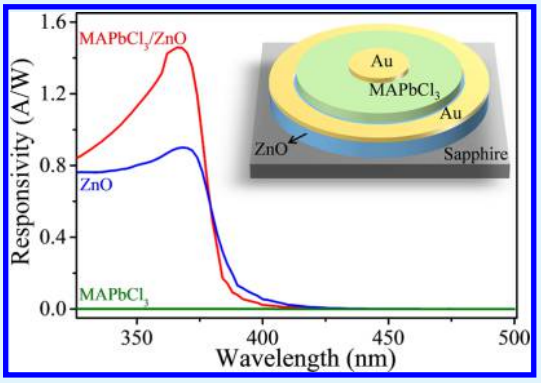

KEYWORDS: *perovskite, ZnO, UV photodetector, transient absorption, electron transfer*

1. INTRODUCTION

Hybrid organic−inorganic perovskites ($MAPbX_3$, MA = CH_3NH_3, X = Cl, Br, or I) have been regarded as one of the most promising candidates for the next-generation optoelectronic devices due to their attractive optical and electrical properties, such as high carrier mobility, long carrier diffusion length, and high light absorption rate.[1−4] In the past few years, the photodetectors based on hybrid organic−inorganic perovskites have made remarkable progress. Different material structures, such as bulk single crystals,[3,5] thin films,[6−8] and nanostructures,[9−11] have been fabricated to demonstrate organic−inorganic perovskites photodetectors. By varying the halide anions (X), the device detection range can be easily tuned from UV to visible range.[12] Notably, the external quantum efficiency (EQE) of organic−inorganic perovskites photodetectors can reach as high as 10^3−10^5, which is conducive to the practical applications.[13−15] However, there is a huge difference in performance among different organic−inorganic perovskites photodetectors, which are extremely sensitive to the preparation conditions.[16,17] Moreover, the photodetectors based on organic−inorganic perovskites always suffer from the rapid deterioration of performance in ambient air due to the unstable nature of the materials.[18] Recently, to solve the above-mentioned problems, combining the organic−inorganic perovskites and the inorganic materials (e.g., ZnO, TiO_2, graphene and WSe_2) together seems like a reliable and effective way for optoelectronic devices.[19−21] For example, by introducing ZnO nanostructures, the detection range of the $CH_3NH_3PbI_3$ photodetectors was greatly extended (from 380 nm UV to 760 nm visible light) with improved responsivity.[22,23] High photoresponsivity and EQE values for hybrid photodetectors consisting of MoS_2 integrated with $CH_3NH_3PbI_3$ can be also clearly achieved.[24] More interestingly, the hybrid devices usually show excellent stability.[25,26] Despite all the above significant progresses, the detailed mechanism of the performance enhancement of these hybrid photodetectors is still not very clear.

Recently, UV photodetectors have drawn much attention for their civil and military applications.[27−30] As is well known, the energy band gaps of $MAPbCl_3$ and ZnO are 3.11 and 3.37 eV, respectively, which make them ideal for UV detection.[31−34] In this work, we demonstrated a $MAPbCl_3$/ZnO hybrid structure and investigated the effect of ZnO on the UV detection performance of $MAPbCl_3$. The ZnO film was synthesized on c-face sapphire by molecular beam epitaxy (MBE) system and then the perovskite layer was deposited onto the ZnO by a

Received: July 13, 2018
Accepted: September 12, 2018
Published: September 12, 2018

DOI: 10.1021/acsami.8b11722
ACS Appl. Mater. Interfaces 2018, 10, 34744−34750

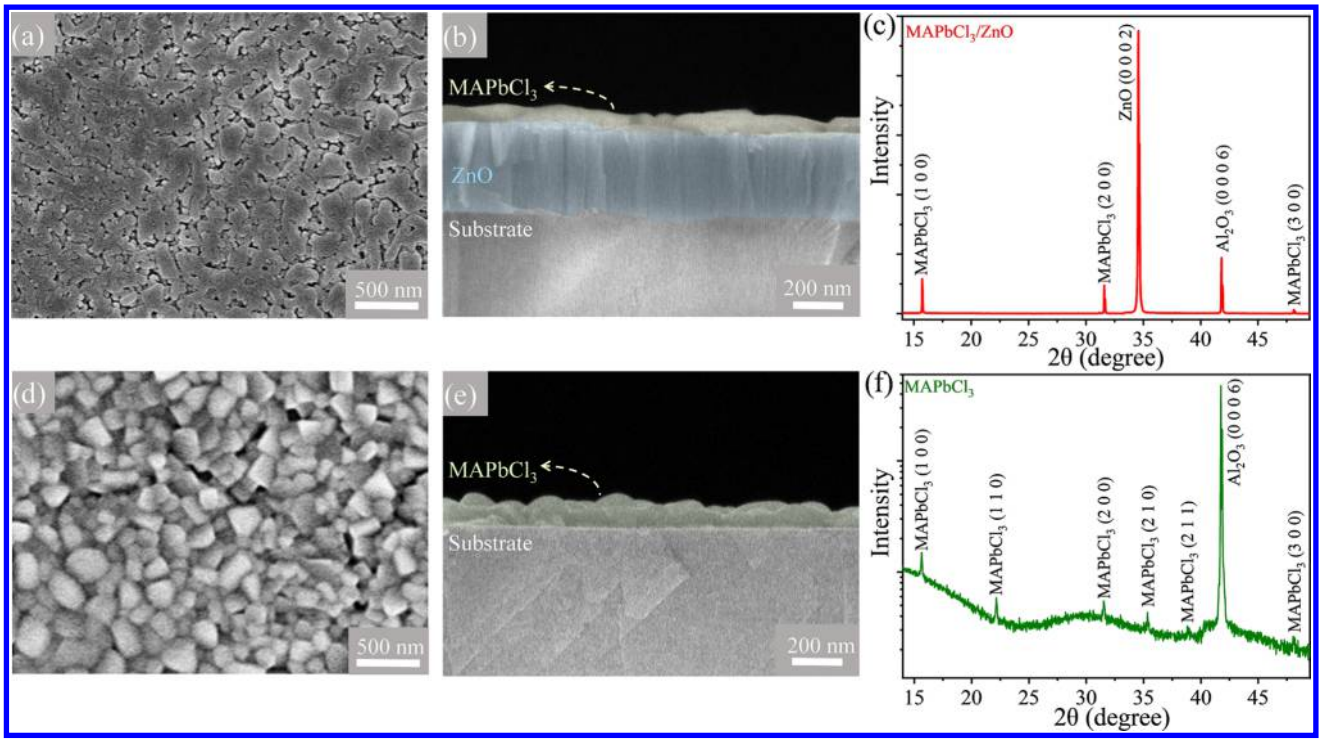

Figure 1. (a) Top-view, (b) cross-sectional SEM images, and (c) XRD pattern of $MAPbCl_3$/ZnO film. (d) Top-view, (e) cross-sectional SEM images, and (f) XRD pattern of $MAPbCl_3$ film.

solution-processing technique. The morphologies, structures, and optical and photoresponse properties of $MAPbCl_3$/ZnO were characterized in detail. The results indicate that the $MAPbCl_3$/ZnO UV photodetector exhibits a higher responsivity and a quicker response speed than pure ZnO and perovskite devices. High crystal quality and low defect density of $CH_3NH_3PbCl_3$ on ZnO film is another important reason for the excellent UV detection performance. Moreover, by analyzing the photoluminescence (PL) spectra, the transient absorption (TA) spectra, and the photoresponse spectra, it can be concluded that the carriers' separation and transfer between $MAPbCl_3$ and ZnO should play an important role in the performance enhancement of $MAPbCl_3$/ZnO UV photodetector. Our investigations provide a promising route to design high-performance photodetectors by controlling the interfaces between perovskite films and semiconductors.

2. EXPERIMENTAL SECTION

2.1. Preparation of ZnO Film. High-quality ZnO film was deposited on c-face sapphire substrate by MBE. 6 N-purity zinc source in thermal Knudsen cell and 5 N-purity O_2 activated in a radio frequency (RF) plasma source were employed. Before the growth of ZnO, the substrates were treated by O_2 plasma at 700 °C for 30 min to remove some surface impurities. Then, ZnO film was grown with the substrate temperature at 650 °C and the pressure of 3×10^{-5} Pa for 4 h. The temperature of zinc source was kept at 210 °C and the RF source power was fixed at 300 W.

2.2. Preparation of $MAPbCl_3$/ZnO Hybrid Structure. Equal mole MACl (98%, Aladdin) and $PbCl_2$ (≥99.0%, Shanghai No. 4 Reagent & H.V. Chemical Limited Company) were dissolved in dimethyl sulfoxide solution. The concentration of MACl and $PbCl_2$ is 0.5 mol/L. Then, the solution was stirred until precursor materials were completely dissolved at room temperature. After that, $MAPbCl_3$ precursor solution was spin-coated on the ZnO film with a rotation rate of 5000 rpm for 20 s. Then, a drop of toluene was spin-coated on the film immediately at the rotation rate of 1000 rpm for 3 s. Subsequently, the sample was put on the hotplate with the temperature of 100 °C for 10 min.

2.3. Characterization and Measurements of the Materials and Devices. The surface morphology and cross-section of the samples were characterized by scanning electron microscope (SEM) (HITACHI S-4800). The surface roughness of ZnO film was estimated by atomic force microscopy (AFM; Bruker, MultiMode-8). The crystal structure was characterized by X-ray diffraction (XRD) (Rigaku) with Cu Kα as the radiation source (λ = 0.154 nm). The transmission and absorption spectra were recorded using a UV-3101PC scanning spectrophotometer. Current−voltage (I−V) curves and time-dependent photocurrent (I−t) curves were measured by semiconductor parameter analyzer (Keithely 2200). The response spectra of the fabricated devices were measured by a 200 W UV-enhanced Xe lamp with a monochromator. The PL measurement was performed at room temperature using He−Cd laser line of 325 nm as an excitation source. The TA spectra were recorded by a pump-probe spectroscopy setup with a Ti:sapphire laser (Spectra-Physics, Spitfire ACE, 800 nm, 4.5 mJ/pulse, full width at half maximum 35 fs, 1 kHz). Pump pulses at 325 nm were generated by an optical parameter amplifier. The white-light probe was generated by the fundamental laser output focused on a CaF_2 window. The angle between polarizations of pump and probe was changed by a $\lambda/2$ wave plate (Thorlabs, AHWP05M-340). The pump pulses were chopped by a synchronized chopper (Newport, model 3502) to 25 Hz. After passing through the sample, the probe beam was focused onto a fiber-coupled spectrometer (Ocean Optics, QE PRO). The group velocity dispersion of the whole experimental system was compensated by a chirp program. All the experiments were performed at room temperature.

3. RESULTS AND DISCUSSION

The surface of ZnO film is flat with a root-mean-square roughness of about 5.96 nm (see Figure S1a). And the crystalline size of ZnO film is estimated to be about 82.2 nm by XRD using Scherrer's equation (see Figure S1b). The top-view and cross-sectional SEM images of $MAPbCl_3$/ZnO film are shown in Figure 1a and b, respectively. The surface of

DOI: 10.1021/acsami.8b11722
ACS Appl. Mater. Interfaces 2018, 10, 34744−34750

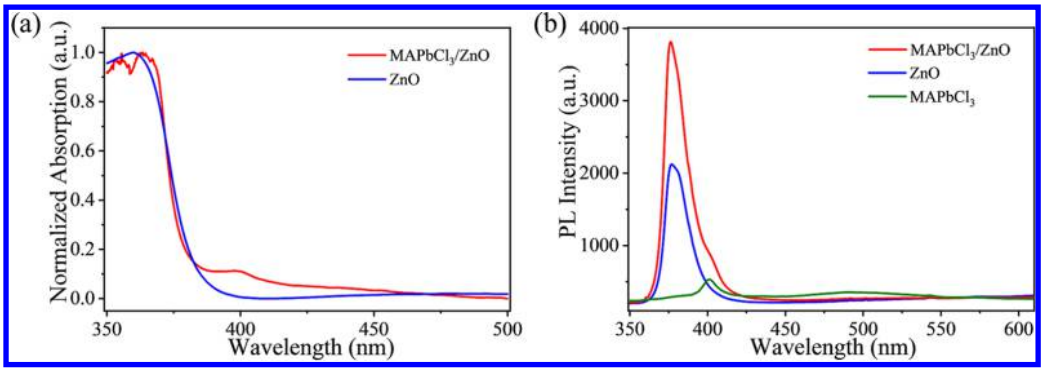

Figure 2. a) Transmission spectra of $MAPbCl_3$/ZnO and pure ZnO films. (b) PL spectra of $MAPbCl_3$/ZnO film, ZnO film, and $MAPbCl_3$ film.

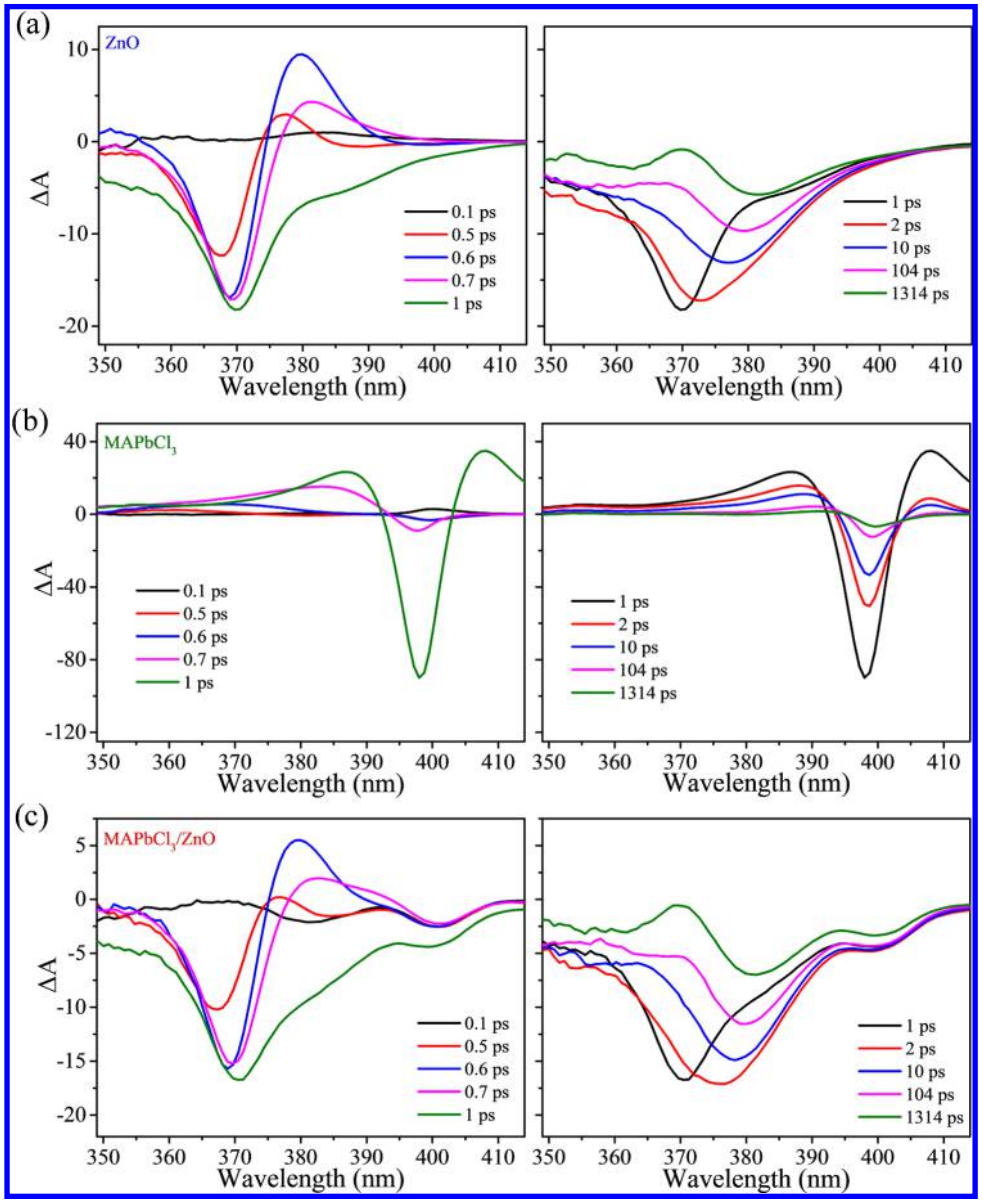

Figure 3. TA spectra of (a) ZnO film, (b) $MAPbCl_3$ film, and (c) $MAPbCl_3$/ZnO film. ΔA is the change in absorption.

$MAPbCl_3$ film on ZnO is also flat and uniform. The cross-sectional SEM image indicates that the thicknesses of ZnO and $MAPbCl_3$ are about 350 and 100 nm, respectively. Figure 1c shows the XRD result of the $MAPbCl_3$/ZnO film on the c-face sapphire substrate. Except the diffraction peaks of the c-sapphire substrate (0006) at 41.81° and wurtzite ZnO(0002) at 34.58°, all other diffraction peaks can be indexed to cubic $MAPbCl_3$. The diffraction peaks located at 2θ = 15.71, 31.60, and 48.12° can be assigned to the (100), (200), and (300) planes of a cubic perovskite structure, respectively.[35] To make

DOI: 10.1021/acsami.8b11722
ACS Appl. Mater. Interfaces 2018, 10, 34744−34750

a comparison, a $MAPbCl_3$ film was prepared directly on the c-sapphire substrate. Figure 1d–f show the top-view and cross-sectional SEM images, as well as the XRD pattern of the $MAPbCl_3$ film on sapphire, respectively. It could be seen that the surface of $MAPbCl_3$ film on sapphire has a rougher surface and more grain boundaries compared with that on ZnO. And the thickness of $MAPbCl_3$ film is also about 100 nm (see Figure 1e). In Figure 1f, the X-ray diffraction peaks of $MAPbCl_3$ film on sapphire at 2θ = 15.71, 22.16, 31.60, 35.34, 38.82, and 48.12° could be attributed to the (100), (110), (200), (210), (221), and (300) planes of the cubic perovskite structure.[35] And the weak peak intensity implies the relatively poor crystallinity of $MAPbCl_3$ film on sapphire.

Figure 2a shows the absorption spectra of the $MAPbCl_3$/ZnO and the pure ZnO films on c-sapphire substrate. Different from that of the pure ZnO, the absorption spectrum of $MAPbCl_3$/ZnO exhibits an obvious absorption band at around 400 nm, which should come from the near band edge (NBE) absorption of $MAPbCl_3$. Figure 2b presents the PL spectra of $MAPbCl_3$/ZnO, ZnO, and $MAPbCl_3$ films. For pure ZnO, a strong narrow PL peak at around 377 nm can be clearly observed, which corresponds to the NBE emission of ZnO. Moreover, nearly no visible emission can be found. After covering with $MAPbCl_3$, the PL peak intensity of NBE UV emission was enhanced obviously. In addition, a small emission shoulder at its longer wavelength side for $MAPbCl_3$/ZnO should come from the NBE emission of $MAPbCl_3$.

To further investigate the carrier dynamics of $MAPbCl_3$/ZnO film, TA spectra measurements were performed at room temperature. Figure 3 shows the TA spectra of ZnO, $MAPbCl_3$, and $MAPbCl_3$/ZnO films recorded at 0–1 and 1–1314 ps after 325 nm excitation. Several features should be noted: (1) negative features at around 365–380 nm (see Figure 3a,c) and 400 nm (see Figure 3b,c) can be assigned to ground-state bleaching (GSB) of the band edge transition of ZnO and $MAPbCl_3$, respectively. (2) For ZnO and $MAPbCl_3$/ZnO films, a positive feature at around 380 nm appears before 1 ps (see Figure 3a,c), which should be induced by excitonic optical Stark effect.[36,37] (3) For $MAPbCl_3$ film, two positive features at around 407 and 390 nm appear in the whole delay time (see Figure 3b), which can be attributed to the band gap renormalization and photoinduced reflection or absorption, respectively.[38]

Figure 4 shows a comparison of the kinetic traces and their fits extracted from the GSB features of $MAPbCl_3$/ZnO, ZnO, and $MAPbCl_3$ films. In Figure 4a, the fitted curve of the kinetics for $MAPbCl_3$ showed two time constants of 0.4 ps (86%) and 22.9 ps (14%). The fast component for this sample is attributed to charge carrier trapping at perovskite grain boundaries. Although the exact origin of the slow component is not definitive, it is most likely from the electron–hole recombination at the band edge. From the fit of the kinetics for $MAPbCl_3$/ZnO, two slower time constants of 0.5 ps (41%) and 83.9 ps (59%) are obtained compared to $MAPbCl_3$. From the XRD and SEM results, it is clear that $MAPbCl_3$ fabricated on ZnO exhibits a higher crystal quality and fewer grain boundaries than Al_2O_3. Therefore, the improvement in the crystal quality and the reduction of grain boundaries should be responsible for the longer recombination time constant for $MAPbCl_3$/ZnO. Of note, in $MAPbCl_3$/ZnO structure, the contribution to the TA signal of electrons injection into ZnO must be considered, which can be further supported by a slower rise in GSB around 370–380 nm for $MAPbCl_3$/ZnO

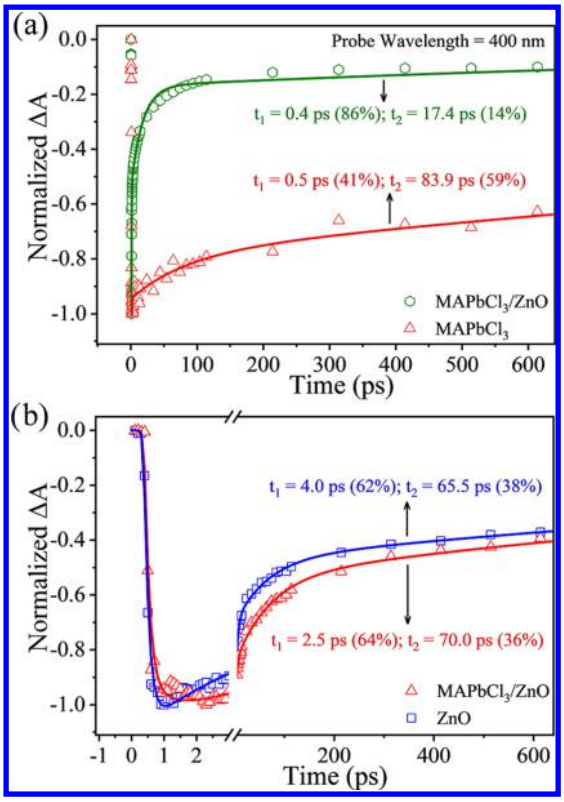

Figure 4. (a) Normalized $MAPbCl_3$ GSB kinetics and their fits of $MAPbCl_3$/ZnO film and $MAPbCl_3$ film. (b) Normalized ZnO GSB kinetics and their fits of $MAPbCl_3$/ZnO film and ZnO film.

than that for pure ZnO, as shown in Figure 4b.[39,40] The injection of electrons into ZnO at the interface could also explain the enhancement of PL intensity at 377 nm for $MAPbCl_3$/ZnO (see Figure 2b). It should be mentioned here that a third component over 1.4 ns exists in all kinetic decay traces in Figure 4. And this long-lifetime component may be associated with electron–hole recombination, which will not be discussed in this work.[41–43]

To investigate the light detection performance of $MAPbCl_3$/ZnO, the vertical structural UV photodetector has been fabricated. Figure 5a illustrates the schematic structure of the device. Both the ring-shaped bottom electrode (3.5 mm inner diameter and 5 mm outer diameter) on ZnO and the round top electrode (1.4 mm diameter) on $MAPbCl_3$ were made of Au with a thickness of 30 nm. Figure 5b shows the I–V curves of the photodetectors based on $MAPbCl_3$/ZnO, $MAPbCl_3$, and ZnO measured in the dark and under 365 nm light irradiation with a light density of 100 $\mu W/cm^2$. As extracted from Figure 5b, after introducing the ZnO layer, the dark current of $MAPbCl_3$ photodetector increased by about 4 orders of magnitude, whereas the photocurrent increased by more than 6 orders of magnitude. In addition, the light ON/OFF ratio at 10 V of $MAPbCl_3$/ZnO photodetector was calculated to be about 2.1×10^2. Figure 5c shows the responsivity curves of $MAPbCl_3$, $MAPbCl_3$/ZnO, and ZnO devices. It could be seen that the −3 dB cutoff wavelength is around 378 nm for both $MAPbCl_3$/ZnO and ZnO devices with a peak responsivity at ~366 nm. Interestingly, by introducing $MAPbCl_3$, the peak responsivity was improved obviously and could reach ~1.47 A/W at 1 V bias with an external quantum efficiency of ~500%. It is well known that the crystal quality and the surface morphology play an

DOI: 10.1021/acsami.8b11722
ACS Appl. Mater. Interfaces 2018, 10, 34744–34750

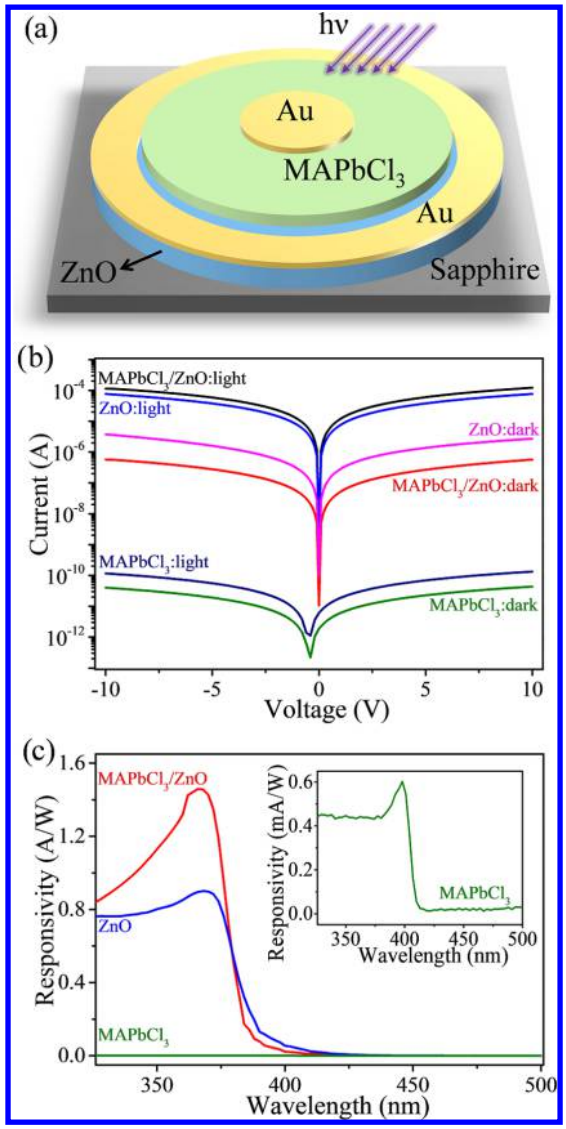

Figure 5. (a) Schematic structure of the $MAPbCl_3$/ZnO UV photodetector. (b) *I*–*V* curves of $MAPbCl_3$/ZnO, ZnO, and $MAPbCl_3$ devices. (c) Response spectra of $MAPbCl_3$/ZnO, ZnO, and $MAPbCl_3$ devices measured at the bias of 1 V, 1 V and 50 V, respectively. The inset figure is the amplified response curve of $MAPbCl_3$ device.

important role in device performance.[14] Therefore, the excellent photoresponse performance of $MAPbCl_3$/ZnO should be associated with the higher crystal quality and the less grain boundaries of $MAPbCl_3$ on ZnO. Moreover, when the $MAPbCl_3$/ZnO device was irradiated by UV light, both perovskite and ZnO could generate photogenerated carriers, resulting in a photocurrent enhancement compared with the pure $MAPbCl_3$ and ZnO devices. Additionally, the process of light detection strongly depends on the carrier separation and collection. Therefore, the photoresponse enhancement could be also attributed to the efficient separation and transfer of carries at the $MAPbCl_3$/ZnO interface, which would reduce the recombination of photoexcited electron–hole pairs. In addition, $MAPbCl_3$ device exhibits a relatively weak response in the ultraviolet region due to the poor crystal quality and large defect density of $MAPbCl_3$ on sapphire.

Response time is also an important parameter of UV photodetectors. To investigate the temporal response of the devices, the *I*–*t* curves were measured under 365 nm light irradiation at 10 V as shown in Figure 6a. Obviously, 10–90%

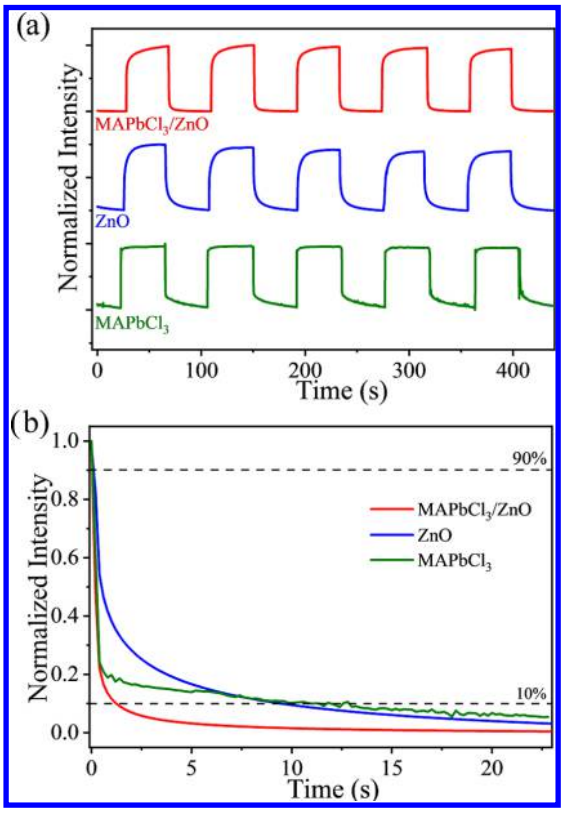

Figure 6. (a) Normalized *I*–*t* curves at a bias of 10 V of $MAPbCl_3$/ZnO, ZnO, and $MAPbCl_3$ devices. (b) Enlarged views of the decay edges of the devices.

rise time of $MAPbCl_3$/ZnO photodetector is around 7.8 s, which is comparable to that of ZnO device (~7.6 s), but a little longer than that of $MAPbCl_3$ device (~0.2 s). Interestingly, compared with the pure ZnO and $MAPbCl_3$ devices, $MAPbCl_3$/ZnO hybrid photodetector shows a shorter 90–10% decay time of ~1.2 s (see Figure 6b). As is well known, perovskites with the low trap density usually have a high carrier mobility and a long carrier-diffusion length.[44] Thus, the quick decay speed of the $MAPbCl_3$/ZnO hybrid device should be associated with the high crystal quality of $MAPbCl_3$ on ZnO. In addition, the quick carriers transfer at the $MAPbCl_3$/ZnO interface can also be responsible for this phenomenon. As for the relatively slow rise time, it may be determined by the generation and recombination process of photogenerated carriers in the ZnO layer.

The stability of $MAPbCl_3$/ZnO has been also investigated. Figure 7 shows the normalized responsivity of $MAPbCl_3$/ZnO device and $MAPbCl_3$ device as a function of storage time. Both devices were stored in the same air ambient with the average temperature of 27 °C and the humidity of 40%. In Figure 7, it could be seen that the responsivity of $MAPbCl_3$ device would decrease to 50% of its original value after 3 days. In contrast, the responsivity of $MAPbCl_3$/ZnO remained nearly constant for more than 10 days. According to the previous reports, fewer defects in hybrid organic–inorganic perovskites would make them more resistant to moisture in ambient air.[45] Therefore, the stability improvement in this work should be

DOI: 10.1021/acsami.8b11722
ACS Appl. Mater. Interfaces 2018, 10, 34744–34750

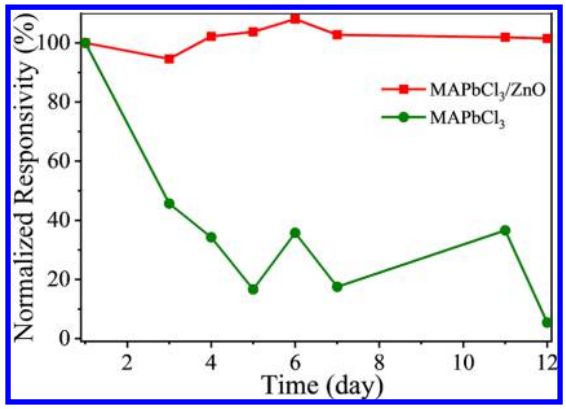

Figure 7. Normalized responsivity of $MAPbCl_3$/ZnO device and $MAPbCl_3$ device as a function of storage time.

associated with the higher crystal quality, flatter surface, and less grain boundaries of the $MAPbCl_3$ film on ZnO.

4. CONCLUSIONS

In summary, we have first demonstrated an UV photodetector based on the $MAPbCl_3$/ZnO heterostructure. By combining $MAPbCl_3$ and ZnO together, the hybrid photodetector exhibits a significantly enhanced responsivity and response speed compared to pure $MAPbCl_3$ and ZnO devices. The responsivity at 365 nm and the 90−10% decay time of $MAPbCl_3$/ZnO hybrid UV photodetector are 1.47 A/W and ∼1.2 s, respectively. In addition, $MAPbCl_3$/ZnO device also shows a better stability compared with $MAPbCl_3$ device. The significantly improved performance of $MAPbCl_3$/ZnO photodetector is mainly attributed to the higher crystal quality of $MAPbCl_3$ on ZnO and the efficient carries' separation and transfer at the $MAPbCl_3$/ZnO interface. The TA and PL results further indicate the process of injection of electrons into ZnO in the $MAPbCl_3$/ZnO heterostructure. Our findings provide insights into the inner properties of perovskite films and the related device performance, which also provide an efficient approach for the fabrication of highly efficient and stable perovskite photodetectors.

■ ASSOCIATED CONTENT

Supporting Information

The Supporting Information is available free of charge on the ACS Publications website at DOI: 10.1021/acsami.8b11722.

(a) AFM and (b) XRD of ZnO film (PDF)

■ AUTHOR INFORMATION

Corresponding Authors

*E-mail: liukw@ciomp.ac.cn (K.L.).
*E-mail: shendz@ciomp.ac.cn (D.S.).

ORCID

Jialin Yang: 0000-0002-9670-0524

Author Contributions

The manuscript was written through contributions of all the authors. All the authors have given approval to the final version of the manuscript.

Notes

The authors declare no competing financial interest.

■ ACKNOWLEDGMENTS

This work is supported by the National Natural Science Foundation of China (61475153, 61605200, 11727902, 61425021, and 61525404), Jilin Province Young and Middle-aged Science and Technology Innovation Leaders and Team Project (20180519023JH), and the 100 Talents Program of the Chinese Academy of Sciences.

■ REFERENCES

(1) Green, M. A.; Ho-Baillie, A.; Snaith, H. J. The Emergence of Perovskite Solar Cells. *Nat. Photonics* **2014**, *8*, 506−514.
(2) Saparov, B.; Mitzi, D. B. Organic-Inorganic Perovskites: Structural Versatility for Functional Materials Design. *Chem. Rev.* **2016**, *116*, 4558−4596.
(3) Yang, S. D.; Fu, W. F.; Zhang, Z. Q.; Chen, H. Z.; Li, C. Z. Recent Advances in Perovskite Solar Cells: Efficiency, Stability and Lead-Free Perovskite. *J. Mater. Chem. A* **2017**, *5*, 11462−11482.
(4) Zhang, S. F.; Zhang, C. M.; Bi, E. B.; Miao, X. L.; Zeng, H. B.; Han, L. Y. Organic-Inorganic Halide Perovskite Solar Cell with $CH_3NH_3PbI_2Br$ as Hole Conductor. *J. Power Sources* **2017**, *339*, 61−67.
(5) Fang, Y. J.; Dong, Q. F.; Shao, Y. C.; Yuan, Y. B.; Huang, J. S. Highly Narrowband Perovskite Single-Crystal Photodetectors Enabled by Surface-Charge Recombination. *Nat. Photonics* **2015**, *9*, 679−686.
(6) Wang, W. Z.; Xu, H. T.; Cai, J.; Zhu, J. B.; Ni, C. W.; Hong, F.; Fang, Z. B.; Xu, F. Z.; Cui, S. W.; Xu, R.; Wang, L. J.; Xu, F.; Huang, J. Visible Blind Ultraviolet Photodetector Based on $CH_3NH_3PbCl_3$ Thin Film. *Opt. Express* **2016**, *24*, 8411−8419.
(7) Zheng, E. J.; Yuh, B.; Tosado, G. A.; Yu, Q. M. Solution-Processed Visible-Blind UV-A Photodetectors Based on $CH_3NH_3PbCl_3$ Perovskite Thin Films. *J. Mater. Chem. C* **2017**, *5*, 3796−3806.
(8) Adinolfi, V.; Ouellette, O.; Saidaminov, M. I.; Walters, G.; Abdelhady, A. L.; Bakr, O. M.; Sargent, E. H. Fast and Sensitive Solution-Processed Visible-Blind Perovskite UV Photodetectors. *Adv. Mater.* **2016**, *28*, 7264−7268.
(9) Jang, D. M.; Park, K.; Kim, D. H.; Park, J.; Shojaei, F.; Kang, H. S.; Ahn, J. P.; Lee, J. W.; Song, J. K. Reversible Halide Exchange Reaction of Organometal Trihalide Perovskite Colloidal Nanocrystals for Full-Range Band Gap Tuning. *Nano Lett.* **2015**, *15*, 5191−5199.
(10) Horváth, E.; Spina, M.; Szekrenyes, Z.; Kamaras, K.; Gaal, R.; Gachet, D.; Forro, L. Nanowires of Methylammonium Lead Iodide ($CH_3NH_3PbI_3$) Prepared by Low Temperature Solution-Mediated Crystallization. *Nano Lett.* **2014**, *14*, 6761−6766.
(11) Gao, L.; Zeng, K.; Guo, J. S.; Ge, C.; Du, J.; Zhao, Y.; Chen, C.; Deng, H.; He, Y. S.; Song, H. S.; Niu, G. D.; Tang, J. Passivated Single-Crystalline $CH_3NH_3PbI_3$ Nanowire Photodetector with High Detectivity and Polarization Sensitivity. *Nano Lett.* **2016**, *16*, 7446−7454.
(12) Zhao, Y.; Zhu, K. Organic-Inorganic Hybrid Lead Halide Perovskites for Optoelectronic and Electronic Applications. *Chem. Soc. Rev.* **2016**, *45*, 655−689.
(13) Wangyang, P.; Gong, C. H.; Rao, G. F.; Hu, K.; Wang, X. P.; Yan, C. Y.; Dai, L. P.; Wu, C. Y.; Xiong, J. Recent Advances in Halide Perovskite Photodetectors Based on Different Dimensional Materials. *Adv. Opt. Mater.* **2018**, *6*, No. 1701302.
(14) Zhou, J. C.; Huang, J. Photodetectors Based on Organic-Inorganic Hybrid Lead Halide Perovskites. *Adv. Sci.* **2018**, *5*, No. 1700256.
(15) Dong, Y. H.; Zou, Y. S.; Song, J. Z.; Song, X. F.; Zeng, H. B. Recent Progress of Metal Halide Perovskite Photodetectors. *J. Mater. Chem. C* **2017**, *5*, 11369−11394.
(16) Kim, J.; Lee, S. H.; Lee, J. H.; Hong, K. H. The Role of Intrinsic Defects in Methylammonium Lead Iodide Perovskite. *J. Phys. Chem. Lett.* **2014**, *5*, 1312−1317.

DOI: 10.1021/acsami.8b11722
ACS Appl. Mater. Interfaces 2018, 10, 34744−34750

(17) Yin, W. J.; Yang, J. H.; Kang, J.; Yan, Y. F.; Wei, S. H. Halide Perovskite Materials for Solar Cells: a Theoretical Review. *J. Mater. Chem. A* **2015**, *3*, 8926−8942.
(18) Wang, D.; Wright, M.; Elumalai, N. K.; Uddin, A. Stability of Perovskite Solar Cells. *Sol. Energy Mater. Sol. Cells* **2016**, *147*, 255−275.
(19) Lu, J.; Carvalho, A.; Liu, H.; Lim, S. X.; Neto, A. H. C.; Sow, C. H. Hybrid Bilayer WSe_2-$CH_3NH_3PbI_3$ Organolead Halide Perovskite as a High-Performance Photodetector. *Angew. Chem., Int. Ed.* **2016**, *55*, 11945−11949.
(20) Lee, Y.; Kwon, J.; Hwang, E.; Ra, C. H.; Yoo, W. J.; Ahn, J. H.; Park, J. H.; Cho, J. H. High-Performance Perovskite-Graphene Hybrid Photodetector. *Adv. Mater.* **2015**, *27*, 41−46.
(21) Li, J.; Yuan, S. H.; Tang, G. Q.; Li, G. J.; Liu, D.; Li, J.; Hu, X. H.; Liu, Y. C.; Li, J. B.; Yang, Z.; Liu, S. Z. F.; Liu, Z. K.; Gao, F.; Yan, F. High-Performance, Self-Powered Photodetectors Based on Perovskite and Graphene. *ACS Appl. Mater. Interfaces* **2017**, *9*, 42779−42787.
(22) Gao, T.; Zhang, Q.; Chen, J. N.; Xiong, X.; Zhai, T. Y. Performance-Enhancing Broadband and Flexible Photodetectors Based on Perovskite/ZnO-Nanowire Hybrid Structures. *Adv. Opt. Mater.* **2017**, *5*, No. 1700206.
(23) Cao, F. R.; Tian, W.; Gu, B. K.; Ma, Y. L.; Lu, H.; Li, L. High-Performance UV-Vis Photodetectors Based on Electrospun ZnO Nanofiber-Solution Processed Perovskite Hybrid Structures. *Nano Res.* **2017**, *10*, 2244−2256.
(24) Bai, F.; Qi, J. J.; Li, F.; Fang, Y. Y.; Han, W. P.; Wu, H. L.; Zhang, Y. A High-Performance Self-Powered Photodetector Based on Monolayer MoS_2/Perovskite Heterostructures. *Adv. Mater. Interfaces* **2018**, *5*, No. 1701275.
(25) Chen, W.; Wu, Y. Z.; Yue, Y. F.; Liu, J.; Zhang, W. J.; Yang, X. D.; Chen, H.; Bi, E. B.; Ashraful, I.; Gratzel, M.; Han, L. Y. Efficient and Stable Large-Area Perovskite Solar Cells with Inorganic Charge Extraction Layers. *Science* **2015**, *350*, 944−948.
(26) You, J.; Meng, L.; Song, T. B.; Guo, T. F.; Yang, Y.; Chang, W. H.; Hong, Z. R.; Chen, H. J.; Zhou, H. P.; Chen, Q.; Liu, Y. S.; De Marco, N.; Yang, Y. Improved Air Stability of Perovskite Solar Cells via Solution-Processed Metal Oxide Transport Layers. *Nat. Nanotechnol.* **2016**, *11*, 75−81.
(27) Zhang, X. L.; Liu, Q. Y.; Liu, B. D.; Yang, W. J.; Li, J.; Niu, P. J.; Jiang, X. Giant UV Photoresponse of a GaN Nanowire Photodetector through Effective Pt Nanoparticle Coupling. *J. Mater. Chem. C* **2017**, *5*, 4319−4326.
(28) Kim, J.; Lee, H. C.; Kim, K. H.; Hwang, M. S.; Park, J. S.; Lee, J. M.; So, J. P.; Choi, J. H.; Kwon, S. H.; Barrelet, C. J.; Park, H. G. Photon-Triggered Nanowire Transistors. *Nat. Nanotechnol.* **2017**, *12*, 963−968.
(29) Zhang, X.; Liu, B.; Liu, Q.; Yang, W.; Xiong, C.; Li, J.; Jiang, X. Ultrasensitive and Highly Selective Photodetections of UV-A Rays Based on Individual Bicrystalline GaN Nanowire. *ACS Appl. Mater. Interfaces* **2017**, *9*, 2669−2677.
(30) Zhang, X.; Liu, B.; Yang, W.; Jia, W.; Li, J.; Jiang, C.; Jiang, X. 3D-Branched Hierarchical 3C-SiC/ZnO Heterostructures for High-Performance Photodetectors. *Nanoscale* **2016**, *8*, 17573−17580.
(31) Baikie, T.; Barrow, N. S.; Fang, Y. A.; Keenan, P. J.; Slater, P. R.; Piltz, R. O.; Gutmann, M.; Mhaisalkar, S. G.; White, T. J. A Combined Single Crystal Neutron/X-ray Diffraction and Solid-State Nuclear Magnetic Resonance Study of the Hybrid Perovskites $CH_3NH_3PbX_3$ (X = I, Br and Cl). *J. Mater. Chem. A* **2015**, *3*, 9298−9307.
(32) Liu, K.; Sakurai, M.; Aono, M. ZnO-Based Ultraviolet Photodetectors. *Sensors* **2010**, *10*, 8604−8634.
(33) Fan, M. M.; Liu, K. W.; Chen, X.; Wang, X.; Zhang, Z. Z.; Li, B. H.; Shen, D. Z. Mechanism of Excellent Photoelectric Characteristics in Mixed-Phase ZnMgO Ultraviolet Photodetectors with Single Cutoff Wavelength. *ACS Appl. Mater. Interfaces* **2015**, *7*, 20600−20606.
(34) Wang, X.; Liu, K. W.; Chen, X.; Li, B. H.; Jiang, M. M.; Zhang, Z. Z.; Zhao, H. F.; Shen, D. Z. Highly Wavelength-Selective Enhancement of Responsivity in Ag Nanoparticle-Modified ZnO UV Photodetector. *ACS Appl. Mater. Interfaces* **2017**, *9*, 5574−5579.
(35) Maculan, G.; Sheikh, A. D.; Abdelhady, A. L.; Saidaminov, M. I.; Hague, M. A.; Murali, B.; Alarousu, E.; Mohammed, O. F.; Wu, T.; Bakr, O. M. $CH_3NH_3PbCl_3$ Single Crystals: Inverse Temperature Crystallization and Visible-Blind UV-Photodetector. *J. Phys. Chem. Lett.* **2015**, *6*, 3781−3786.
(36) Deschler, F.; Price, M.; Pathak, S.; Klintberg, L. E.; Jarausch, D. D.; Higler, R.; Huttner, S.; Leijtens, T.; Stranks, S. D.; Snaith, H. J.; Atature, M.; Phillips, R. T.; Friend, R. H. High Photoluminescence Efficiency and Optically Pumped Lasing in Solution-Processed Mixed Halide Perovskite Semiconductors. *J. Phys. Chem. Lett.* **2014**, *5*, 1421−1426.
(37) Omae, K.; Kawakami, Y.; Fujita, S.; Yamada, M.; Narukawa, Y.; Mukai, T. Effects of Internal Electric Field and Carrier Density on Transient Absorption Spectra in a Thin GaN Epilayer. *Phys. Rev. B* **2002**, *65*, No. 073308.
(38) Price, M. B.; Butkus, J.; Jellicoe, T. C.; Sadhanala, A.; Briane, A.; Halpert, J. E.; Broch, K.; Hodgkiss, J. M.; Friend, R. H.; Deschler, F. Hot-Carrier Cooling and Photoinduced Refractive Index Changes in Organic-Inorganic Lead Halide Perovskites. *Nat. Commun.* **2015**, *6*, No. 8420.
(39) Marchioro, A.; Teuscher, J.; Friedrich, D.; Kunst, M.; van de Krol, R.; Moehl, T.; Gratzel, M.; Moser, J. E. Unravelling the Mechanism of Photoinduced Charge Transfer Processes in Lead Iodide Perovskite Solar Cells. *Nat. Photonics* **2014**, *8*, 250−255.
(40) Xing, G.; Mathews, N.; Sun, S. Y.; Lim, S. S.; Lam, Y. M.; Gratzel, M.; Mhaisalkar, S.; Sum, T. C. Long-Range Balanced Electron- and Hole-Transport Lengths in Organic-Inorganic $CH_3NH_3PbI_3$. *Science* **2013**, *342*, 344−347.
(41) Wang, L.; McCleese, C.; Kovalsky, A.; Zhao, Y.; Burda, C. Femtosecond Time-Resolved Transient Absorption Spectroscopy of $CH_3NH_3PbI_3$ Perovskite Films: Evidence for Passivation Effect of PbI_2. *J. Am. Chem. Soc.* **2014**, *136*, 12205−12208.
(42) Chen, Q.; Zhou, H. P.; Song, T. B.; Luo, S.; Hong, Z. R.; Duan, H. S.; Dou, L. T.; Liu, Y. S.; Yang, Y. Controllable Self-Induced Passivation of Hybrid Lead Iodide Perovskites toward High Performance Solar Cells. *Nano Lett.* **2014**, *14*, 4158−4163.
(43) Stranks, S. D.; Eperon, G. E.; Grancini, G.; Menelaou, C.; Alcocer, M. J. P.; Leijtens, T.; Herz, L. M.; Petrozza, A.; Snaith, H. J. Electron-Hole Diffusion Lengths Exceeding 1 Micrometer in an Organometal Trihalide Perovskite Absorber. *Science* **2013**, *342*, 341−344.
(44) Ahmadi, M.; Wu, T.; Hu, B. A Review on Organic-Inorganic Halide Perovskite Photodetectors: Device Engineering and Fundamental Physics. *Adv. Mater.* **2017**, *29*, No. 1605242.
(45) Xu, X.; Zhang, X.; Deng, W.; Huang, L.; Wang, W.; Jie, J.; Zhang, X. Saturated Vapor-Assisted Growth of Single-Crystalline Organic-Inorganic Hybrid Perovskite Nanowires for High-Performance Photodetectors with Robust Stability. *ACS Appl. Mater. Interfaces* **2018**, *10*, 10287−10295.

DOI: 10.1021/acsami.8b11722
ACS Appl. Mater. Interfaces 2018, 10, 34744−34750